Full length article

Competition between formation of carbides and reversed austenite during tempering of a medium-manganese steel studied by thermodynamic-kinetic simulations and atom probe tomography

A. Kwiatkowski da Silva, G. Inden, A. Kumar, D. Ponge[*], B. Gault, D. Raabe

Max-Planck Institut für Eisenforschung, Max-Planck Str. 1, 40237 Düsseldorf, Germany

ABSTRACT

We investigated the thermodynamics and kinetics of carbide precipitation in a cold-rolled Fe-7Mn-0.1C-0.5Si medium manganese steel during low temperature tempering. The material was annealed up to 24 h at 450 °C in order to follow the kinetics of precipitation. Using thermodynamics and kinetics simulations, we predicted the growth of $M_{23}C_6$ carbides according to the local-equilibrium negligible partition (LENP) mode where carbide growth is controlled by the diffusion of carbon, while maintaining local chemical equilibrium at the interface. Atom-probe tomography (APT) measurements performed on samples annealed for 1, 6 and 24 h at 450 °C confirmed that LENP is indeed the mode of carbide growth and that Mn segregation is necessary for the nucleation. Additionally, we observed the heterogeneous nucleation of transition carbides with a carbon content between 6 and 8 at% at segregated dislocations and grain boundaries. We describe these carbides as a complex face-centered cubic transition carbide type (CFCC-TmC phase) obtained by the supersaturation of the FCC structure by carbon that will act as precursor to the more stable γ-$M_{23}C_6$ carbide that forms at the dislocations and grain boundaries. The results suggest that the addition of carbon does not directly favor the formation of austenite, since Mn is consumed by the formation of the carbides and the nucleation of austenite is thus retarded to later stages of tempering as every FCC nucleus in the initial stages of tempering is readily converted into a carbide nucleus. We propose the following sequence of transformation: (i) carbon and Mn co-segregation to dislocations and grain boundaries; (ii) formation of FCC transition carbides; (iii) growth controlled according to the LENP mode and (iv) austenite nucleation and growth.

© 2018 Acta Materialia Inc. Published by Elsevier Ltd. All rights reserved.

1. Introduction

Medium manganese steels (4—12 wt % Mn) emerge as candidate alloys for the third generation of advanced high strength steels (AHSS), since they combine high strength and ductility with low material costs [1—6]. Their microstructure is typically composed of a cubic α' martensite (matrix) and some retained and/or reversed austenite obtained after intercritical annealing (reversion heat-treatment) [2,7—11]. A wide range of mechanical properties can be obtained for these alloys by tuning the thermomechanical treatment and hence the dispersion and stability of the austenite [1,12—17]. The choice of the optimum thermomechanical processing for tuning these alloys for specific mechanical properties

requires precise knowledge of the thermodynamics and kinetics of the formation of austenite and secondary phases such as carbides and nitrides [18—21].

Mn segregation to defects plays a key role in the austenite reversion [15,22—24]. More specific segregation to lattice defects such as dislocations and interfaces alters the chemical composition locally and hence the thermodynamic driving force for phase nucleation at decorated defects [25,26]. This concept has been successfully applied to the design of martensitic medium manganese steels with high strength and ductility via the reversion of austenite [18—20,22,27,28]. Comparably little attention has been placed on unveiling the role of segregation for the formation of other phases, e.g. ultra-fine carbides, and how the precipitation of these different phases competes with the process or martensite-to-austenite reversion [29]. Indeed, the structural and chemical characterization of ultra-fine/nano-sized precipitates is very challenging especially regarding identification of phases with similar

crystal structure such as FCC carbides. Complex face centered cubic transition-metal carbides (CFCC-TmC) are carbides that are formed with transition metals from the 3d block. All these carbides assume cubic structure with rather similar lattice parameters (in the range of 1.0–1.1 nm) [30]. γ-$M_{23}C_6$ and η-M_6C are the best-known carbides of this type, being widely reported in Cr-, Mn- and Mo-alloyed stainless steels [30,31]. A detailed *ab-initio* study about the stability and structure of these carbides was performed by Fang et al. [30], where they predicted high stability at 0 K for the γ-$M_{23}C_6$ and η-M_6C, and instability for the π-$M_{11}C_2$ phases.

Here we investigate the thermodynamics and kinetics of the precipitation of the $M_{23}C_6$ carbide in a cold-rolled Fe-7Mn-0.1C-0.5Si (wt. %) medium Mn steel upon tempering at 450 °C. Understanding the mechanisms of formation of alloyed carbides such as $M_{23}C_6$ is important in order to elucidate the role of carbon on the nucleation of reversed austenite in medium Mn steels. Both phenomena occur preferably at solute decorated grain boundaries. More specific, we followed the sequence of phase transformation from the early stages of tempering in order to understand the influence of manganese and carbon segregation to grain boundaries and their role on the kinetics and thermodynamics of the formation of both, carbide and austenite. The results suggest that the addition of carbon does not directly favor the formation of austenite, since Mn is consumed by the formation of the carbides and the nucleation of austenite is thus retarded to later stages of tempering as every FCC nucleus in the initial stages of tempering is readily converted into a carbide nucleus. As will be discussed below in more detail we refer to this effect as carbon poisoning of reversed austenite formation.

2. Materials and methods

Details of alloy synthesis and processing are given in Refs. [32,33]. A 30 kg ingot of a medium manganese Fe-7Mn-0.1C-0.5Si (wt.%) steel was cast in a vacuum induction furnace. The composition of the ingot was measured by wet chemical analysis and is Fe-7.22Mn-0.093C-0.49Si-0.013Al-0.005P-0.007S (wt.%). The material was homogenized during 12 h at 1150 °C in an Ar-rich atmosphere, and subsequently hot-rolled to a ~5.5-mm thick plate at temperatures ranging from ~1100 °C to 900 °C, and then air-quenched down to room temperature. The hot-rolled specimen in the as-quenched state showed a martensitic microstructure without retained austenite. The hot-rolled plate was ~55% cold-rolled to ~2.0-mm thick sheets. The material was subsequently annealed for 1 h, 6 h, 24 h and 2 weeks at 450 °C in order to follow the kinetics of carbide precipitation and austenite reversion. The temperature of 450 °C was selected in order to follow the kinetics of precipitation of $M_{23}C_6$ and its effect on the austenite reversion, since both are stable phases at this temperature according to the bulk phase diagram (Fig. 1). Fig. 1a shows a pseudo-binary phase diagram for the Fe7Mn0.5SixC (wt.%) alloy composition and Fig. 1b shows an isothermal section at 450 °C of the Fe-Mn-C system. Both diagrams were calculated using Thermocalc in conjunction with the TCFE9 database.

In order to follow the kinetics of nucleation and growth of the $M_{23}C_6$ carbides, we conducted APT measurements of the samples annealed after 1 h, 6 h and 24 h. Needle-shaped APT specimens were prepared using a FEI Helios Nanolab 600i dual-beam FIB/SEM instrument. The specimens were extracted from the surface of the bulk material using the FIB lift-out procedure suggested by Thompson et al., [34], mounted on the top of commercial Si microtips, and sharpened by annular ion milling. APT was performed on a LEAP 5000 XS (straight flight path) at a base temperature of 60 K in laser-pulsed mode at 40 pJ pulse energy. The wavelength, pulse rate and detection rate of the laser were 355 nm, 500 kHz and 1.5%,

respectively. Reconstruction was carried out using commercial software (Cameca IVAS®) following the protocol introduced by Geiser et al. [35]. Transmission electron microscopy (TEM) investigations were conducted on a FIB-prepared sample in a Philips CM20 with a LaB6 filament operated at 200 kV. The samples were further characterized by high-resolution X-ray diffraction (XRD) using a Seifert Type ID3003 Diffractometer and Co-$K_{\alpha 1}$ radiation ($\lambda = 1.78897$ Å). The scanning range, rate and step size were 20–130°, 20s/step and 0.03°, respectively. The weight percentage of austenite was calculated using the Rietveld simulation method performed with the software BRUKER TOPAS Version 5.0.

Tensile testing was performed after 55% cold rolling and tempering for 6 and 24 h at 450 °C using a Kammrath and Weiss stage. The strain was measured by digital image correlation (DIC) using the Aramis software (GOM GmbH). Three flat samples were analyzed in total from each tempering condition at room temperature and an initial strain rate of 10^{-3} s^{-1}. The thickness, width and gauge length of the samples were 1 mm, 5 mm and 25 mm respectively.

Thermodynamics and kinetics calculations were performed using the software Thermo-Calc in conjunction with the TCFE9 database. Details of the models used in this database can be found in Refs. [36–38]. The kinetics simulations were performed using the diffusion module (DICTRA) [39–41] implemented in Thermo-Calc together with the MOBFE4 database for the mobility of the elements in body-centered-cubic (BCC) Fe. Details about the mobility data in BCC-Fe can be found in Refs. [42–44]. The mobility of Mn in the BCC phase was enhanced by a factor of 45 in order to mimic the behaviour of the martensitic matrix owing to its high defect density enabling higher Mn mobility [27]. $M_{23}C_6$ was considered in the model as a phase without internal diffusion due to the lack of diffusion data for this phase. The DICTRA simulations were performed assuming spherical cell boundary conditions with a radius of 100 nm. The simulations were started using a 2 nm radius spherical carbide region adjacent to the ferrite (BCC) region.

3. Results

3.1. Microstructure characterization

3.1.1. Analysis after 1 h tempering at 450 °C

Fig. 2 shows two APT reconstructions from the Fe7Mn0.5Si0.1C (wt.%) alloy annealed for 1 h at 450 °C. At this stage of tempering, we already observed segregation of C and Mn to dislocations and grain boundaries. The segregation of Mn is highlighted by the 9 at% Mn yellow iso-composition surfaces in Fig. 2a and b. In addition to the segregation of Mn and C, two types of features can be distinguished in the microstructure. Fig. 2a shows a composition profile as a function of the distance to the selected iso-composition surfaces (referred to as proximity histogram or proxigram [45]) obtained from the particles highlighted by the red circles in the first APT reconstruction. The C fraction in these small precipitates is similar to the composition of the $M_{23}C_6$ carbide (20.7 at% C) and the Mn content is higher than 40 at%. Fig. 2b shows an average proxigram obtained from the particles highlighted by red circles in the second APT reconstruction. This second group of features has a similar Mn content to the one in Fig. 2a, but the carbon content is around 5 to 8 at.%. This second group can be regarded as an embryo stage of the more stable $M_{23}C_6$ carbide, since their composition is still below the composition of the critical nucleus of $M_{23}C_6$ and they are probably already organized into a FCC structure due to the high Mn content. We used here a typical and rather common definition of an embryo as a cluster of atoms organized as a new phase until it has reached a critical size or composition as also suggested by typical textbooks in this field [46].
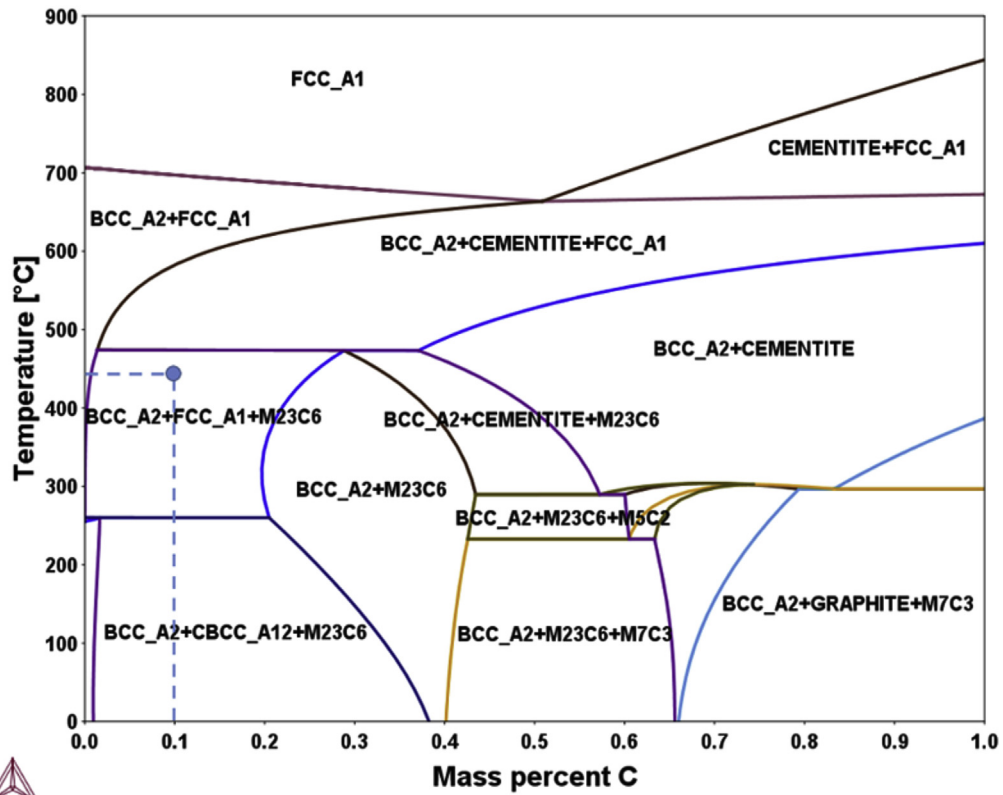
(a)
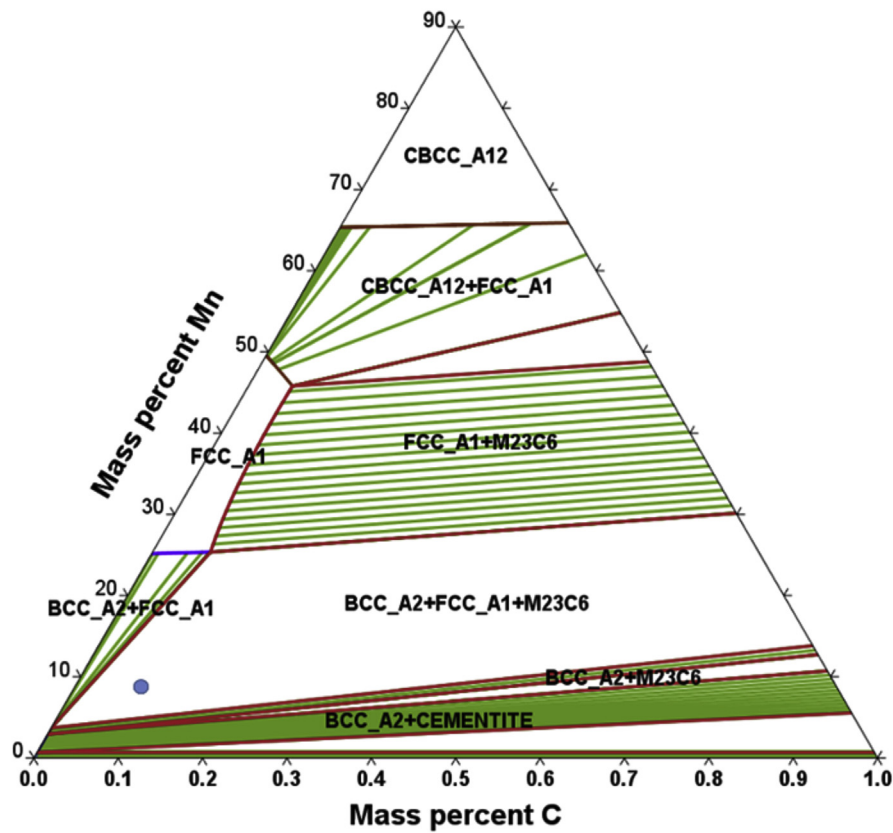
(b)

Fig. 1. (a) Pseudo-binary phase diagram for the Fe7Mn0.5SixC (wt.%) alloy composition. (b) Fe-Mn-C ternary phase diagram: isothermal section at 450 °C.
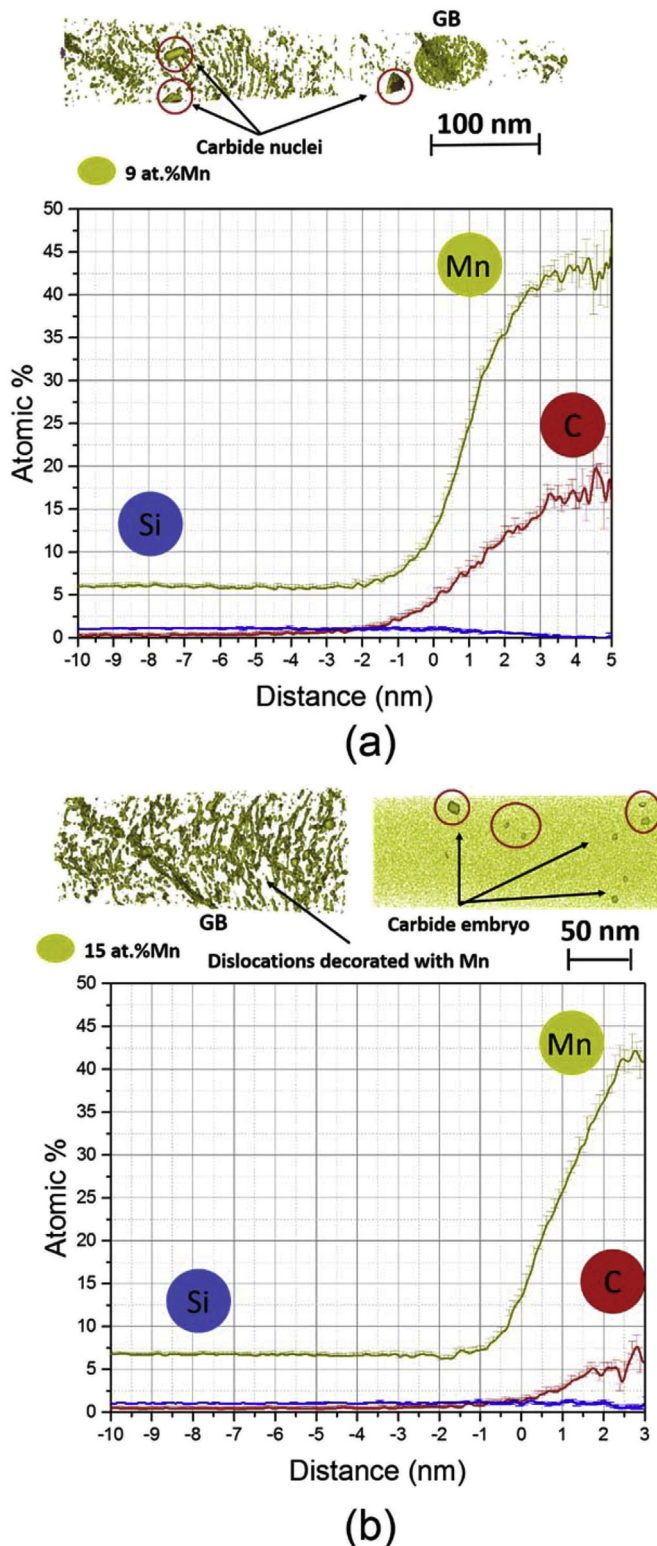
Fig. 2. APT analysis: Fe7Mn0.5Si0.1C (wt.%) alloy, 55% cold-rolled and subsequently tempered at 450 °C for 1 h. (a) Proxigram obtained from the carbides with near M23C6 composition. (b) Proxigram obtained from the carbides with low carbon content.

3.1.2. Analysis after 6 h tempering at 450 °C

We subsequently analyzed the Fe7Mn0.5Si0.1C (wt.%) alloy annealed for 6 h at 450 °C. In the APT tomographic reconstruction shown in Fig. 3a, we can identify carbides with a $M_{23}C_6$

composition, similar to those in Fig. 2a. These carbides are 20–30 nm in size. The carbon content inside the carbide is similar to the carbon content in the carbide of Fig. 2a, as indicated by the proxigram in Fig. 3b. These carbides do not show strong partitioning of Mn to their interior. This can also be clearly visualized by extracting a region of interest of the APT dataset (blue box in Fig. 3a). The Mn ions within this region-of-interest are shown in Fig. 3c and a Mn composition profile is shown in Fig. 3d. The Mn enrichment in the interface is around 55 at% and confined to a region around 2 nm. We observed as well for this condition the formation of embryos of carbides similar to the ones shown in Fig. 2. These embryos are shown in Fig. 4.

Fig. 4a and b respectively show 8.5 at%Mn and 25 at%Mn iso-composition surfaces visualized within the same dataset. By comparing Fig. 4a and b we find that the particles made visible in terms of the 25 at% isosurface were nucleated from dislocations that were highlighted by the 8.5 at% isocomposition surface in Fig. 4a. Fig. 4c shows in detail these particles being formed on the intersection of two dislocations. Such features as shown in Fig. 4a at dislocations have been revealed in a similar material in previous works by using correlative TEM and APT [47,48]. Fig. 4d shows a proxigram calculated using the isosurfaces from Fig. 4b. These particles contain around 8 at%C and 48 at%Mn and they seem to be nucleating at locations where dislocations intersect. This specific composition does not match any known stable carbide, indicating that they are transition carbides and/or represent an embryonic precursor stage in the formation of the $M_{23}C_6$ carbides observed in the microstructures by APT.

Next we performed TEM probing on the sample tempered at 450 °C for 6 h in order to characterize the regions of precipitation of the carbides. The results are shown in Fig. 5. The microstructure of the material is typical for a cold-rolled martensitic steel. We detect formation of very fine precipitates (<20 nm) along grain boundaries and dislocations. These precipitates are indicated by the blue arrows in Fig. 5. The areas of precipitation match the ones observed by APT. It was not possible to obtain crystallographic information from these precipitates due to their small size.

3.1.3. Analysis after 24 h tempering at 450 °C

We conducted further APT analysis on samples annealed for 24 h at 450 °C. Fig. 6 summarizes the results obtained at this tempering stage. Fig. 6a shows an APT dataset containing a M23C6 carbide with size around 40 nm at a grain boundary. Fig. 6b shows a detailed chemical profile of this precipitate obtained from the region-of-interest (blue box) displayed in Fig. 6a. The composition of this carbide is very similar to the ones displayed in Fig. 3, but the distinct compositional shell surrounding the particle in direct local contact and equilibrium with the adjacent matrix extends to around 10 nm in this case. The grain boundary pinned by the precipitate still contains an excess of solute compared to the matrix. We identified as well the presence of smaller carbides associated with dislocations and grain boundaries, as shown in Fig. 6c. The composition of these precipitates is shown in Fig. 6d through an average proxigram calculated for all the carbides displayed in Fig. 6c. These carbides have $M_{23}C_6$ composition as well and seem to have formed from the transition carbides shown in Fig. 4 for 6 h of annealing time. However, in contrast to the carbides shown in Fig. 6a, these carbides are much smaller. This suggests that they are stable nuclei that experience no further growth (possibly due to the limited amount of carbon available in the matrix after this time of tempering).

Additionally, we followed the evolution of the microstructure by X-ray diffraction (XRD). Although the resolution of XRD is limited for the characterization of the $M_{23}C_6$ carbides due to their small volume fraction (around 1.8% in equilibrium), the technique is
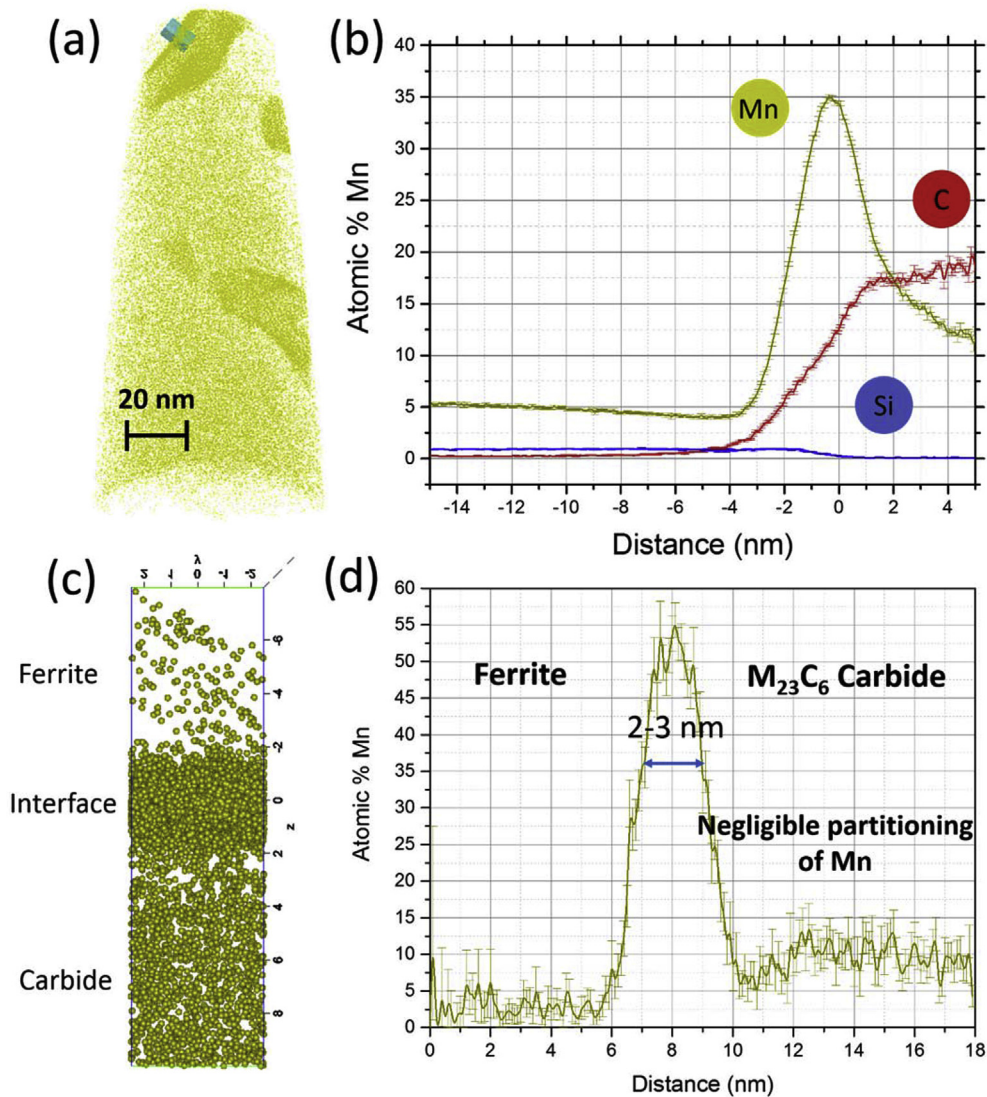
Fig. 3. APT analysis: Fe7Mn0.5Si0.1C (wt.%) alloy, 55% cold-rolled and subsequently tempered at 450 °C for 6 h (a) APT reconstruction: only Mn atoms are displayed. (b) Proxigram obtained from the carbides displayed in (a). (c) and (d): detailed analysis of the region of interest (blue box) displayed in (a). (c) only Mn atom are visualized: we that the Mn-rich interface region has a size of 2–3 nm. (d) 1-D concentration profile of the region of interest displaying the concentration of the interface, the negligible partition of Mn to inside the carbide and the Mn depletion zones (in ferrite and inside the carbide). (For interpretation of the references to colour in this figure legend, the reader is referred to the Web version of this article.)

suitable for the characterization of the volume fraction of austenite, which is predicted to be around 9.6% (9.5% in weight fraction) in equilibrium. Fig. 7 shows the XRD patterns of the material at room temperature after 50% cold-rolling and tempering at 450 °C for 6 h, 24 h and 2 weeks. No diffraction peak of austenite was identified for the samples annealed for 6 and 24 h, while the sample annealed for 2 weeks presented an increased austenite weight fraction of 8% (as calculated using the Rietveld simulation method). These results together with the APT experiments suggest that the nucleation and growth of the $M_{23}C_6$ precedes the nucleation and growth of austenite and that the formation of $M_{23}C_6$ and austenite is not taking place simultaneously.

3.2. Mechanical behaviour

Fig. 8 shows the result of two tensile tests performed at room temperature at a strain rate of 10^{-3} s^{-1} on the 55% cold-rolled and

subsequently tempered (6 h and 24 h at 450 °C) Fe7Mn0.5Si0.1C (wt.%) steel. The material shows recovery after 6 and 24 h of annealing, but no strain hardening was observed. The absence of strain hardening indicates that no significant amount of austenite had been reverted from the martensite.

4. Thermodynamics and kinetics simulations

In order to describe the observed sequence of phase transformations, we first calculated the expected phases at equilibrium for the Fe7Mn0.5Si0.1C (wt.%) alloy composition at different temperatures. Fig. 9a presents the Thermo-Calc calculations for the molar fractions in equilibrium as a function of temperature for the different phases, namely, cementite (M_3C), ferrite (BCC_A2), austenite (FCC_A1) and $M_{23}C_6$. The calculations show that both $M_{23}C_6$ and cementite M_3C can precipitate from the BCC matrix depending on temperature. Fig. 9b shows the Gibbs free energy of
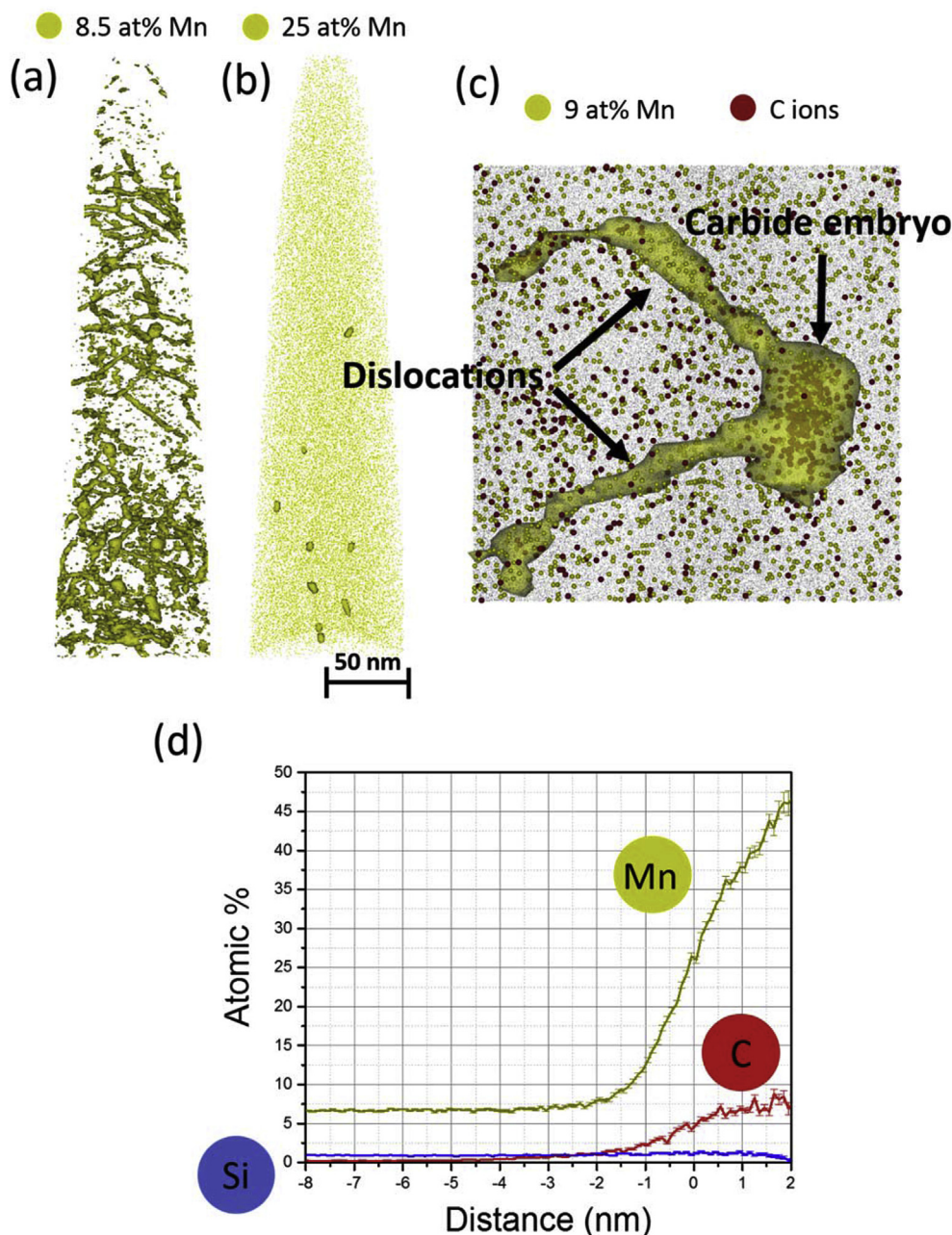
Fig. 4. APT analysis: Fe7Mn0.5Si0.1C (wt.%) alloy, 55% cold-rolled and subsequently tempered at 450 °C for 6 h (a) 8.5 at% Mn isosurfaces revealing the dislocations with Mn segregation. (b) 25 at% Mn isosurfaces revealing the small carbides nucleating from the dislocations. (c) Detail of the carbide embryo being formed on the intersection of two dislocations. (d) Proxigram obtained from the isosurfaces displayed in (b): the small carbides nucleating from the dislocations have C around 8 at%.

the different carbides ($M_{23}C_6$, cementite, M_7C_3 and M_5C_2) and the BCC phase (with the given alloying composition) as a function of the Mn content at 450 °C. We can clearly see that none of the carbides can precipitate from the BCC matrix by a paraequilibrium reaction controlled only by C. Mn-enrichment is necessary in order to form the first nucleus and grow the carbides, as confirmed by our present results. Therefore, the driving force to nucleate these carbides from a BCC matrix can be calculated from the tie-lines for the local-equilibrium (LE) between the carbide and the BCC structure. In this particular case, $M_{23}C_6$ has a higher driving force to precipitate as illustrated by the tie-line displayed in Fig. 9b.

From these considerations we learn that $M_{23}C_6$ has to grow by maintaining the LE at the interface. Nevertheless, C still moves much faster than Mn, which suggests that more free-energy can be dissipated by LENP mode growth rather than by a LE mode of growth. We also performed DICTRA simulations in order to better understand the kinetics of growth of the carbide. The simulation was performed using a 2 nm radius spherical region attached to a ferrite region with 300 nm radius and Fe7Mn0.1C (wt.%) composition. The mobility of Mn in BCC was enhanced by a factor of 45 because the dislocation-rich substructure of this material seems to enable faster mean Mn transport and also this value showed good agreement between experiments and simulations for the growth of austenite at the same temperature in a previous work [19]. $M_{23}C_6$
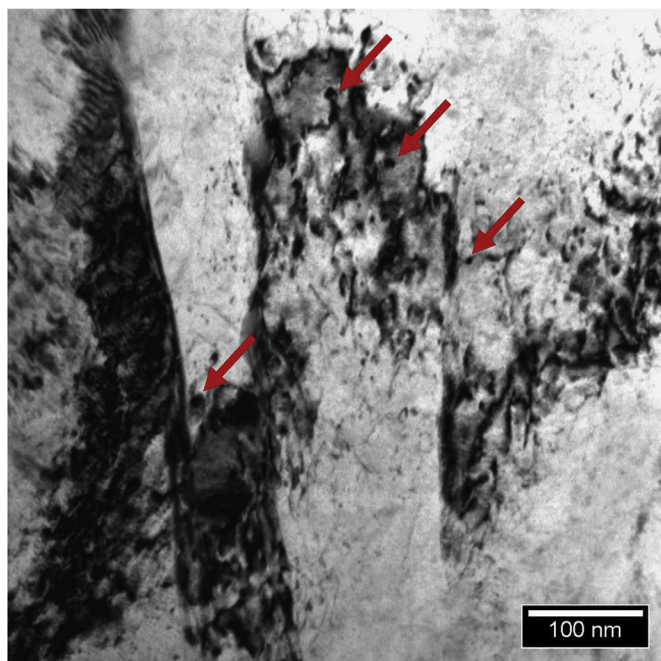
Fig. 5. Bright-field TEM image. Fe7Mn0.5Si0.1C (wt.%) alloy, 55% cold-rolled and subsequently tempered at 450 °C for 6 h. The blue arrows indicate particles precipitated on dislocations and at grain boundaries. (For interpretation of the references to colour in this figure legend, the reader is referred to the Web version of this article.)

was considered as a phase without diffusion and Si was not included in the simulation due to the lack of diffusion data for this phase. The result of the simulation after 3.13s is shown in Fig. 10. The simulation predicts a LENP mode of growth for the $M_{23}C_6$ carbide. The growth is controlled by carbon diffusion, while local equilibrium is maintained at the interface, as indicated by the high Mn spike on the right hand side of the carbide region. The Mn spike on the left-hand side of Fig. 10 shows the composition of the critical nucleus of $M_{23}C_6$, i.e., the composition at which the chemical potential of Mn in $M_{23}C_6$ is equal to the chemical potential of Mn in the super-saturated BCC matrix. This value is in good agreement with the composition of the particles observed after 24 h and shown in Fig. 6 that did not yet experience further growth. These particles can thus be regarded as a critical nucleus of the $M_{23}C_6$ carbide.

5. Discussion

We identified the formation of carbides highly enriched with Mn after 1 h and 6 h at 450 °C. These precipitates have a carbon content around 8 at.%. The results after 24 h clearly indicate that these particles will eventually transform to $M_{23}C_6$ carbides, indicating that these are gamma transition carbides and precursors to the stable $M_{23}C_6$ carbide. Fang et al. [30] calculated from first principles by using density functional theory (DFT) the stability and structure of the different CFCC-TmC phases (CFCC: complex face-centered cubic transition carbide). They predicted high stability for the η-M_6C and γ-$M_{23}C_6$ phases for Mn and Cr-rich host phases. A summary of the calculated formation energies of η'-$M_{12}C$, η-M_6C and γ-$M_{23}C_6$ at 0 K is given in Fig. 11. The dashed lines represent the measured C composition range for the smaller and bigger carbides as measured by APT. We observed by APT carbides with η'-$M_{12}C$ composition (smaller ones) and $M_{23}C_6$ composition (bigger ones).

This observation can be explained in terms of the higher entropy of mixing of the η'-$M_{12}C$ as compared with η-M_6C. Here we propose that η'-$M_{12}C$ carbides are transition carbides to the $M_{23}C_6$ one. Both $M_{12}C$ and M_6C are complex face-centered cubic transition metal carbides, i.e. transition carbides whose structure can be derived from the face-centered-cubic structure. In order to nucleate the $M_{23}C_6$, the nucleus has to pass by different stages of metastability. Our results suggest that strong partitioning of Mn is required during the stage of nucleation of the $M_{23}C_6$. The formation of smaller carbides can be explained by assuming the effect of carbon on the Gibbs free energy of FCC and, as a consequence, on the equilibrium between FCC and BCC. Fig. 12 illustrates such a case. Fig. 12a shows the effect of carbon on the Gibbs free energy of FCC_A1. By increasing the amount of carbon in FCC, the free energy of FCC is increased and, as a consequence, more Mn has to partition to FCC in order to minimize the free energy of FCC. Fig. 12b shows schematically how the addition of 8 at% of carbon shifts the LE between BCC and FCC to higher amounts of Mn. Naturally, when the carbon content in FCC is increasing, some type of ordering of the carbon atoms is required in order to reduce the free energy of the embryo. We can assume that these intermediate stages of ordering occurring before the $M_{23}C_6$ composition is reached are different transition carbides like M_6C and $M_{12}C$ in a cascade of transitional metastability states.

The APT results strongly suggest that Mn and C segregation to grain boundaries and dislocations plays a key role for the nucleation of $M_{23}C_6$. The Mn-rich nuclei observed at short tempering times strongly indicates that strong Mn partitioning is required to nucleate $M_{23}C_6$. On the other hand, bigger carbides observed at later stages of tempering strongly support the thermodynamics and kinetics predictions of a LENP reaction for the growth of the $M_{23}C_6$ carbide. From the above considerations, we propose the following mechanism for the formation of $M_{23}C_6$ carbides:

   i. Gibbsian equilibrium-driven co-segregation of C and Mn to grain boundaries and dislocations. The segregation of carbon to grain-boundaries and dislocations decreases locally the activity of Mn and, as consequence, the segregation of Mn is enhanced by the presence of carbon.
  ii. The increase of the local compositional fluctuations of Mn and C along grain boundaries and dislocations promotes formation of a first FCC embryo. This first embryo has to be highly enriched in Mn in order to form. We designated as *embryo* the group of features with a carbon content in the range of 5–8 at.% observed in the samples after 0.5 and 6 h of annealing. These particles cannot be regarded yet as a nucleus of $M_{23}C_6$, since their composition is still below the composition of the critical nucleus of $M_{23}C_6$.
 iii. Carbon strongly partitions to the FCC embryo. The enrichment of C will eventually lead to the formation of η'-$M_{12}C$ carbides that is a metastable state before the formation of the nucleus of the more stable $M_{23}C_6$ carbide. This is also supported by the APT observations, viz. that the particles with $M_{12}C$ composition located at dislocations and GBs evolve later into particles with $M_{23}C_6$ composition.
  iv. Once the critical nucleus of the $M_{23}C_6$ carbide is formed, the precipitate can grow by a LENP reaction, i.e., the precipitate grows with negligible partitioning (NP) of substitutional solute elements, while the local equilibrium (LE) is maintained at the interface.
   v. Mn partitions to the interior of the carbide during extended heat treatments (homogenization of the carbide composition).
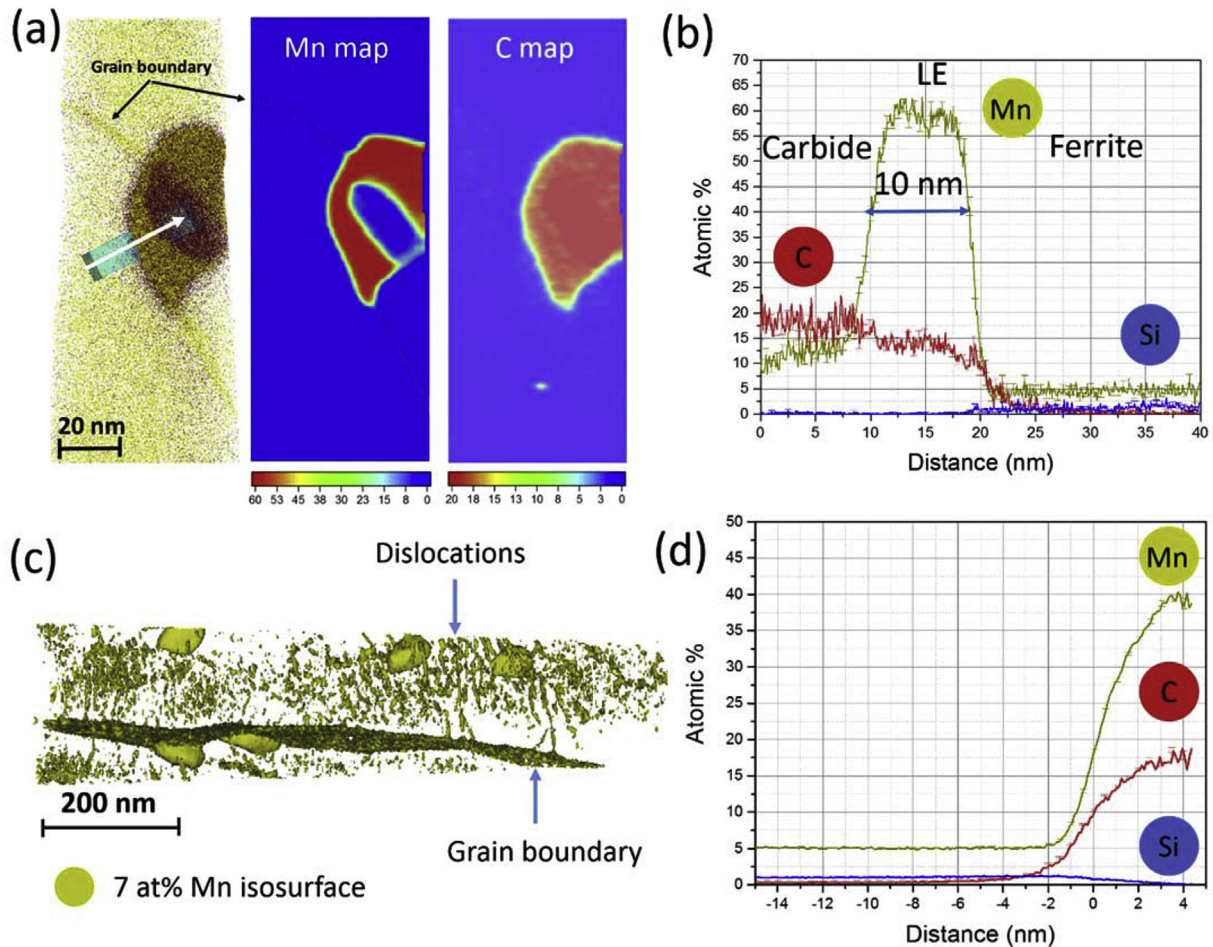
Fig. 6. APT analysis: Fe7Mn0.5Si0.1C (wt.%) alloy, 55% cold-rolled and subsequently tempered at 450 °C for 24 h. (a) Atom-probe reconstruction displaying carbon (brown) and manganese (yellow) ions together with 2D concentration plots of C and Mn: we observe the thickening of the region in local equilibrium near the interface and the existence of some solute excess in the grain boundary. (b) Detailed 1D concentration profile of the region of interest displayed in (a). (c) 7 at% Mn isosurfaces showing the formation of carbides from the dislocations and grain boundary. (d) Proxygram obtained from the carbides displayed through the isosurfaces in (c). LE: local equilibrium. (For interpretation of the references to colour in this figure legend, the reader is referred to the Web version of this article.)
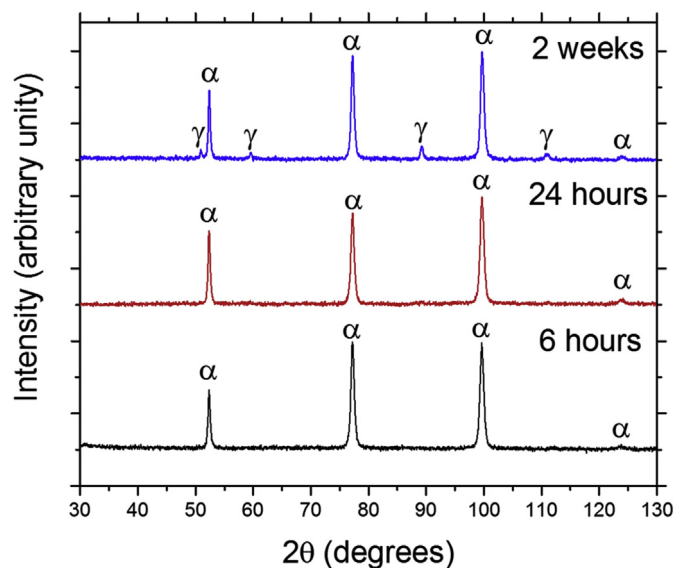

Fig. 7. XRD patterns of the material at room temperature after 50% cold-rolling and tempering at 450 °C for 6 h, 24 h and 2 weeks. Austenite was detected only for the sample tempered after 2 weeks with a weight fraction of 8%.
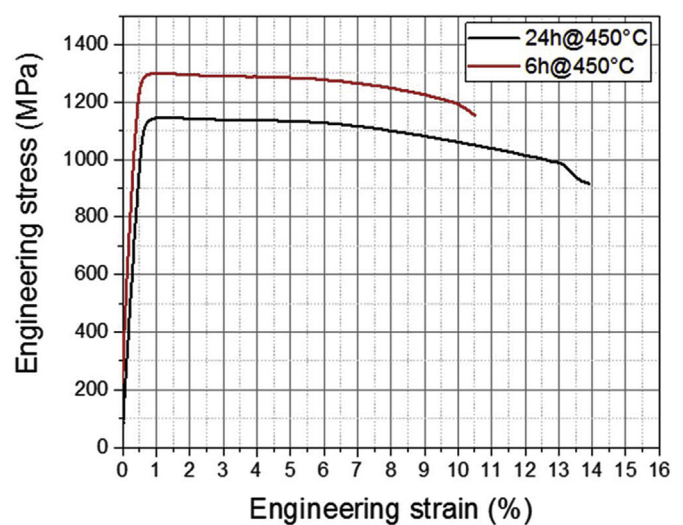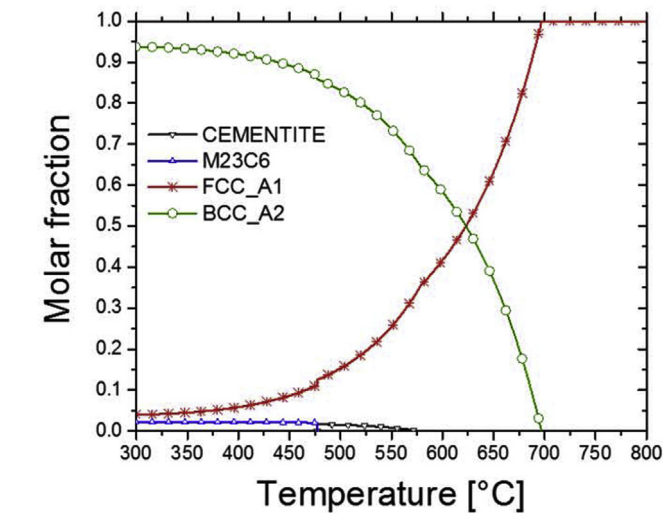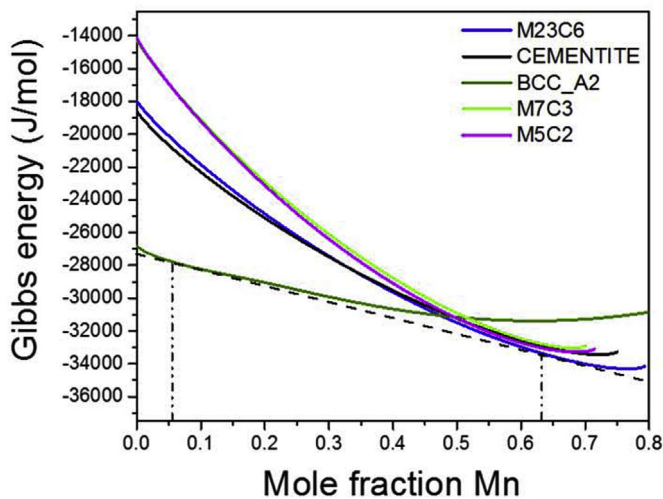
Fig. 8. Stress-strain curve of the material at room temperature after 50% cold-rolling and tempering at 450 °C for 6 h and 24 h prior to testing. The material shows recovery after 6 and 24 h of annealing, but no strain hardening.

(a)

(b)

Fig. 9. Thermo-Calc simulation. (a) Equilibrium molar fraction of different phases as a function of temperature. (b) Gibbs energy of the BCC_A2 matrix with the Fe0.5Si0.1CxMn composition and the Gibbs energy of the different carbides at 450 °C as a function of the Mn content.

Fig. 10. Dictra simulation after 3.13s of simulation time. The simulation was performed using a 2 nm radius spherical region attached to a ferrite region with 300 nm radius and Fe7Mn0.1C (wt.%) composition at 450 °C. $M_{23}C_6$ was inserted as a diffusion none phase. LE: local equilibrium. The Mn-content in $M_{23}C_6$ is the same as that in martensite. The step in the mole-fraction diagram comes from the difference in C-content.

Fig. 11. Calculated formation energies for a carbide M_mC_n, at T = 0 K and P = 0 Pa. The circles represent Mn-phases and squares Fe-phases. The carbon concentration x = n/(m + n). The dashed lines represent the measured C composition range for the smaller and bigger carbides. Data obtained from Ref. [30].

vi. As a consequence of ii) to v), austenite will start to nucleate and grow at much later stages, as compared with an alloy without carbon. While carbon is still present in the BCC matrix, every possible austenite embryo being formed would be first converted into a carbide nucleus rather than maturing into a viable austenite nucleus. When there is not enough carbon to enable the embryo to evolve into $M_{23}C_6$, the same can grow normally as an austenite phase. As a consequence, austenite is effectively nucleated at much later stages, when the BCC matrix is already depleted in C. In this context, we can conclude that the presence of C rather poisons than promotes the nucleation of austenite. Another effect, perhaps less important, relates to the reduction of the amount of Mn that is available for the growth of austenite,
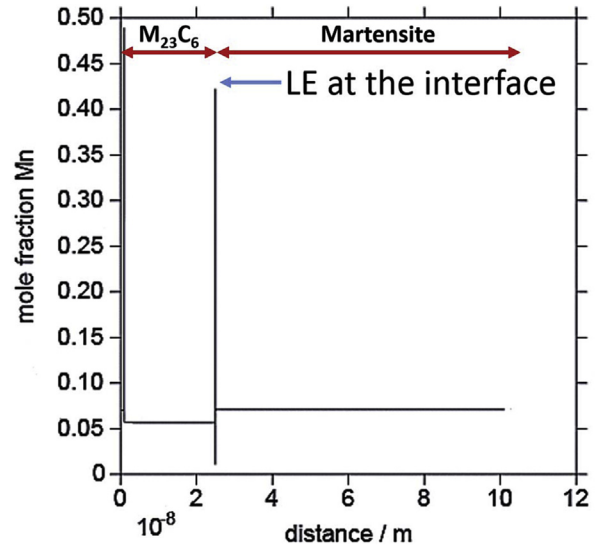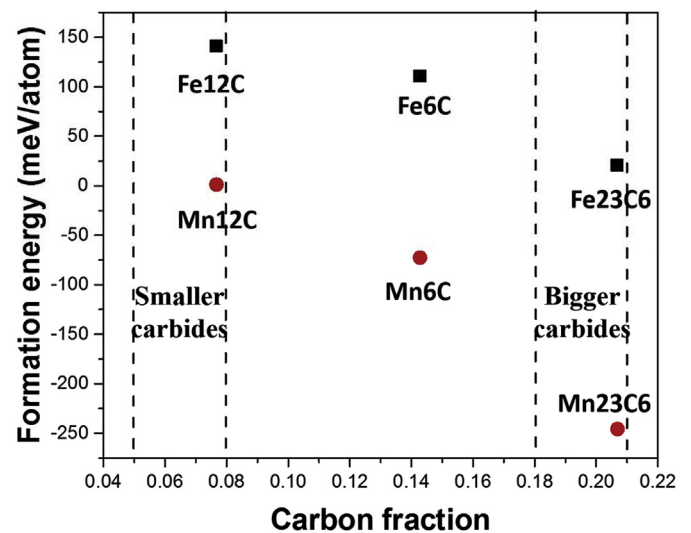
since this element is being consumed for the homogenization of the composition of the $M_{23}C_6$ carbides.

6. Conclusions

The mechanism of precipitation of $M_{23}C_6$ carbides during the different stages of tempering of a medium Mn martensite was described by thermodynamics and kinetics simulations and followed experimentally by APT. Co-segregation of Mn and C is required as a precondition for the formation of the $M_{23}C_6$ carbide, which is preceded by the formation of metastable FCC carbides. Once the first nucleus is formed, $M_{23}C_6$ growth will proceed by a
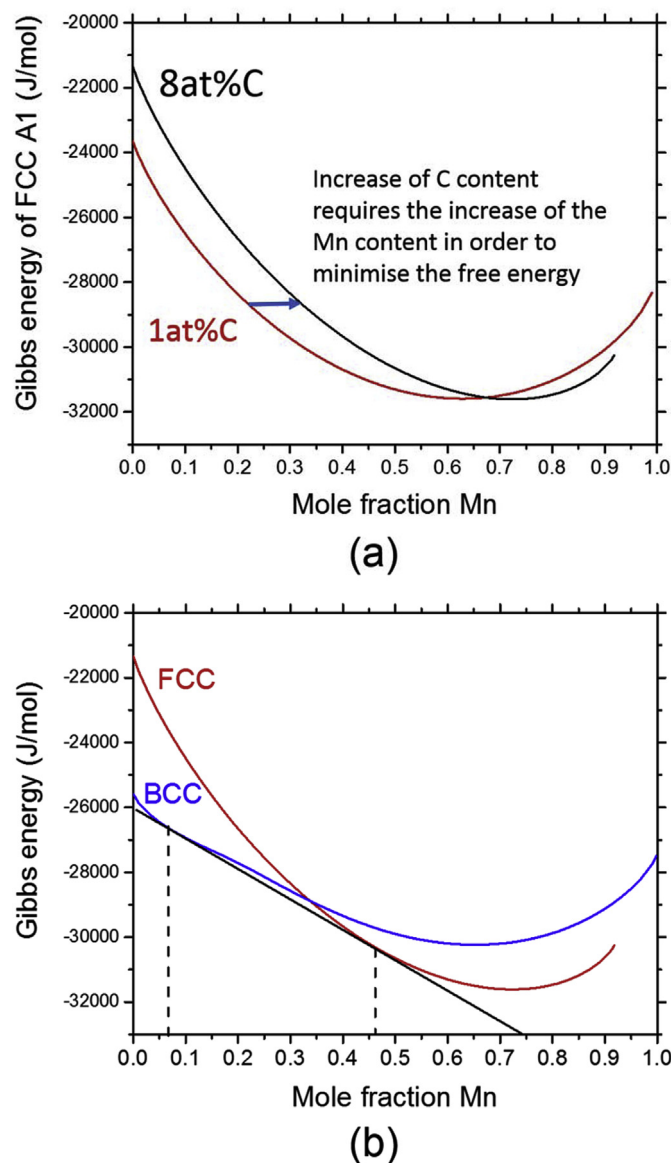
Fig. 12. Effect of carbon on the amount of Mn in austenite. (a) Increase of the free energy of FCC due to the increase in the amount of carbon. (b) Schematic representation of the shift of the amount of Mn in FCC due to the increase of the amount of carbon.

LENP reaction. The homogenization of the Mn content inside the carbide will occur after extended periods of tempering. The nucleation of austenite is belated due to the formation of the carbides, indicating that C poisons the nucleation of austenite at lower temperatures.

References

[1] Y.K. Lee, J. Han, Current opinion in medium manganese steel, Mater. Sci. Technol. 31 (7) (2015) 843—856.

[2] N. Nakada, K. Mizutani, T. Tsuchiyama, S. Takaki, Difference in transformation behavior between ferrite and austenite formations in medium manganese steel, Acta Mater. 65 (Supplement C) (2014) 251—258.

[3] D.W. Suh, J.H. Ryu, M.S. Joo, H.S. Yang, K. Lee, H. Bhadeshia, Medium-alloy manganese-rich transformation-induced plasticity steels, Metall. Mat. Transac. A Phys. Metall. Mat. Sci. 44A (1) (2013) 286—293.

[4] S.J. Lee, S. Lee, B.C. De Cooman, Martensite transformation of sub-micron retained austenite in ultra-fine grained manganese transformation-induced plasticity steel, Int. J. Mater. Res. 104 (5) (2013) 423—429.

[5] S. Lee, B.C. De Cooman, Influence of carbide precipitation and dissolution on the microstructure of ultra-fine-grained intercritically annealed medium manganese steel, Metall. Mat. Transac. A Phys. Metall. Mat. Sci. 47A (7) (2016) 3263—3270.

[6] B.B. He, B. Hu, H.W. Yen, G.J. Cheng, Z.K. Wang, H.W. Luo, M.X. Huang, High dislocation density—induced large ductility in deformed and partitioned steels, Science 357 (6355) (2017) 1029—1032.

[7] S. Takaki, K.L. Ngo-Huynh, N. Nakada, T. Tsuchiyama, Strengthening mechanism in ultra low carbon martensitic steel, ISIJ Int. 52 (4) (2012) 710—716.

[8] N. Nakada, T. Tsuchiyama, S. Takaki, N. Miyano, Temperature dependence of austenite nucleation behavior from lath martensite, ISIJ Int. 51 (2) (2011) 299—304.

[9] A. Holden, J.D. Bolton, E.R. Petty, Structure and properties of iron-manganese alloys, J. Iron Steel Inst. 209 (SEP) (1971), 721-&.

[10] J.D. Bolton, E.R. Petty, G.B. Allen, Mechanical properties of alpha-phase low-carbon fe-mn alloys, Metall. Transac. 2 (10) (1971), 2915-&.

[11] J.D. Bolton, E.R. Petty, G.B. Allen, Influence of austenitizing treatment on structure and mechanical properties of iron-manganese martensite, J. Iron Steel Inst. 207 (1969), 1314-&.

[12] D.W. Suh, S.J. Kim, Medium Mn transformation-induced plasticity steels: recent progress and challenges, Scripta Mater. 126 (2017) 63—67.

[13] H. Springer, M. Belde, D. Raabe, Combinatorial design of transitory constitution steels: coupling high strength with inherent formability and weldability through sequenced austenite stability, Mater. Des. 90 (2016) 1100—1109.

[14] M.I. Latypov, S. Shin, B.C. De Cooman, H.S. Kim, Micromechanical finite element analysis of strain partitioning in multiphase medium manganese TWIP plus TRIP steel, Acta Mater. 108 (2016) 219—228.

[15] H.F. Xu, J. Zhao, W.Q. Cao, J. Shi, C.Y. Wang, C. Wang, J. Li, H. Dong, Heat treatment effects on the microstructure and mechanical properties of a medium manganese steel (0.2C-5Mn), Mat. Sci. Eng. A Struct. Mat. Prop. Microstruct. Process. 532 (2012) 435—442.

[16] H.F. Xu, J. Zhao, W.Q. Cao, J. Shi, C.Y. Wang, J. Li, H. Dong, Tempering effects on the stability of retained austenite and mechanical properties in a medium manganese steel, ISIJ Int. 52 (5) (2012) 868—873.

[17] W.Q. Cao, C. Wang, J. Shi, M.Q. Wang, W.J. Hui, H. Dong, Microstructure and mechanical properties of Fe-0.2C-5Mn steel processed by ART-annealing, Mat. Sci. Eng. A Struct. Mat. Prop. Microstruct. Process. 528 (22—23) (2011) 6661—6666.

[18] D. Raabe, D. Ponge, O. Dmitrieva, B. Sander, Nanoprecipitate-hardened 1.5 GPa steels with unexpected high ductility, Scripta Mater. 60 (12) (2009) 1141—1144.

[19] O. Dmitrieva, D. Ponge, G. Inden, J. Millán, P. Choi, J. Sietsma, D. Raabe, Chemical gradients across phase boundaries between martensite and austenite in steel studied by atom probe tomography and simulation, Acta Mater. 59 (1) (2011) 364—374.

[20] D. Raabe, D. Ponge, O. Dmitrieva, B. Sander, Designing ultrahigh strength steels with good ductility by combining transformation induced plasticity and martensite aging, Adv. Eng. Mater. 11 (7) (2009) 547—555.

[21] J. Bratberg, J. Ågren, K. Frisk, Diffusion simulations of MC and M7C3 carbide coarsening in bcc and fcc matrix utilising new thermodynamic and kinetic description, Mater. Sci. Technol. 24 (6) (2008) 695—704.

[22] M. Kuzmina, D. Ponge, D. Raabe, Grain boundary segregation engineering and austenite reversion turn embrittlement into toughness: example of a 9 wt.% medium Mn steel, Acta Mater. 86 (2015) 182—192.

[23] Y.P. Lu, B. Hutchinson, D.A. Molodov, G. Gottstein, Effect of deformation and annealing on the formation and reversion of epsilon-martensite in an Fe-Mn-C alloy, Acta Mater. 58 (8) (2010) 3079—3090.

[24] K. Grönhagen, J. Ågren, Grain-boundary segregation and dynamic solute drag theory—a phase-field approach, Acta Mater. 55 (3) (2007) 955—960.

[25] D. Raabe, S. Sandloebes, J. Millan, D. Ponge, H. Assadi, M. Herbig, P.P. Choi, Segregation engineering enables nanoscale martensite to austenite phase transformation at grain boundaries: a pathway to ductile martensite, Acta Mater. 61 (16) (2013) 6132—6152.

[26] D. Raabe, M. Herbig, S. Sandloebes, Y. Li, D. Tytko, M. Kuzmina, D. Ponge, P.P. Choi, Grain boundary segregation engineering in metallic alloys: a pathway to the design of interfaces, Curr. Opin. Solid State Mater. Sci. 18 (4) (2014) 253—261.

[27] M.M. Wang, C.C. Tasan, D. Ponge, A. Kostka, D. Raabe, Smaller is less stable: size effects on twinning vs. transformation of reverted austenite in TRIP-maraging steels, Acta Mater. 79 (2014) 268—281.

[28] M.M. Wang, C.C. Tasan, D. Ponge, A.C. Dippel, D. Raabe, Nanolaminate

transformation-induced plasticity-twinning-induced plasticity steel with dynamic strain partitioning and enhanced damage resistance, Acta Mater. 85 (2015) 216—228.

[29] L. Yuan, D. Ponge, J. Wittig, P. Choi, J.A. Jimenez, D. Raabe, Nanoscale austenite reversion through partitioning, segregation and kinetic freezing: example of a ductile 2 GPa Fe-Cr-C steel, Acta Mater. 60 (6—7) (2012) 2790—2804.

[30] C.M. Fang, M.A. van Huis, H.W. Zandbergen, Stability and structures of the CFCC-TmC phases: a first-principles study, Comput. Mater. Sci. 51 (1) (2012) 146—150.

[31] K.H. Lo, C.H. Shek, J.K.L. Lai, Recent developments in stainless steels, Mater. Sci. Eng. R Rep. 65 (4) (2009) 39—104.

[32] J. Han, J.-H. Nam, Y.-K. Lee, The mechanism of hydrogen embrittlement in intercritically annealed medium Mn TRIP steel, Acta Mater. 113 (2016) 1—10.

[33] J. Han, A.K. da Silva, D. Ponge, D. Raabe, S.-M. Lee, Y.-K. Lee, S.-I. Lee, B. Hwang, The effects of prior austenite grain boundaries and microstructural morphology on the impact toughness of intercritically annealed medium Mn steel, Acta Mater. 122 (2017) 199—206.

[34] K. Thompson, D. Lawrence, D.J. Larson, J.D. Olson, T.F. Kelly, B. Gorman, In situ site-specific specimen preparation for atom probe tomography, Ultra-microscopy 107 (2—3) (2007) 131—139.

[35] B.P. Geiser, D.J. Larson, E. Oltman, S. Gerstl, D. Reinhard, T.F. Kelly, T.J. Prosa, Wide-Field-of-View atom probe reconstruction, Microsc. Microanal. 15 (2009) 292—293.

[36] D. Djurovic, B. Hallstedt, J. von Appen, R. Dronskowski, Thermodynamic assessment of the Mn-C system, Calphad Comput. Coupling Phase Diagrams Thermochem. 34 (3) (2010) 279—285.

[37] D. Djurovic, B. Hallstedt, J. von Appen, R. Dronskowski, Thermodynamic assessment of the Fe-Mn-C system, Calphad Comput. Coupling Phase Diagrams Thermochem. 35 (4) (2011) 479—491.

[38] W.M. Huang, An assessment of the Fe-Mn system, Calphad Comput. Coupling Phase Diagrams Thermochem. 13 (3) (1989) 243—252.

[39] A. Borgenstam, L. Höglund, J. Ågren, A. Engström, DICTRA, a tool for simulation of diffusional transformations in alloys, J. Phase Equil. 21 (3) (2000) 269.

[40] A. Schneider, G. Inden, Simulation of the kinetics of precipitation reactions in ferritic steels, Acta Mater. 53 (2) (2005) 519—531.

[41] G. Inden, P. Neumann, Simulation of diffusion controlled phase transformations in steels, Steel Res. 67 (1996) 401—407.

[42] B. Jonsson, C and N diffusion in bcc Cr-Fe-Ni, Metallkunde 85 (1994) 498—501.

[43] B. Jonsson, Cr, Co, Fe and Ni diffusion in bcc Fe, Metallkunde 83 (1992) 349—355.

[44] S.W. Deng, W.M. Chen, J. Zhong, L.J. Zhang, Y. Du, L. Chen, Diffusion study in bcc_A2 Fe-Mn-Si system: experimental measurement and CALPHAD assessment, Calphad Comput. Coupling Phase Diagrams Thermochem. 56 (2017) 230—240.

[45] O.C. Hellman, J.A. Vandenbroucke, J. Rüsing, D. Isheim, D.N. Seidman, Analysis of three-dimensional atom-probe data by the proximity histogram, Microsc. Microanal. 6 (5) (2000) 437—444.

[46] H.I. Aaronson, M. Enomoto, J.K. Lee, Mechanisms of Diffusional Phase Transformations in Metals and Alloys, 2010.

[47] M. Kuzmina, M. Herbig, D. Ponge, S. Sandlöbes, D. Raabe, Linear complexions: confined chemical and structural states at dislocations, Science 349 (6252) (2015) 1080—1083.

[48] A. Kwiatkowski da Silva, G. Leyson, M. Kuzmina, D. Ponge, M. Herbig, S. Sandlöbes, B. Gault, J. Neugebauer, D. Raabe, Confined chemical and structural states at dislocations in Fe-9wt%Mn steels: a correlative TEM-atom probe study combined with multiscale modelling, Acta Mater. 124 (2017) 305—315.